

# *Discrete geometric approach for modelling quantization effects in nanoscale electron devices*

**Alan Paussa, Ruben Specogna, David Esseni & Francesco Trevisan**

**Journal of Computational Electronics**

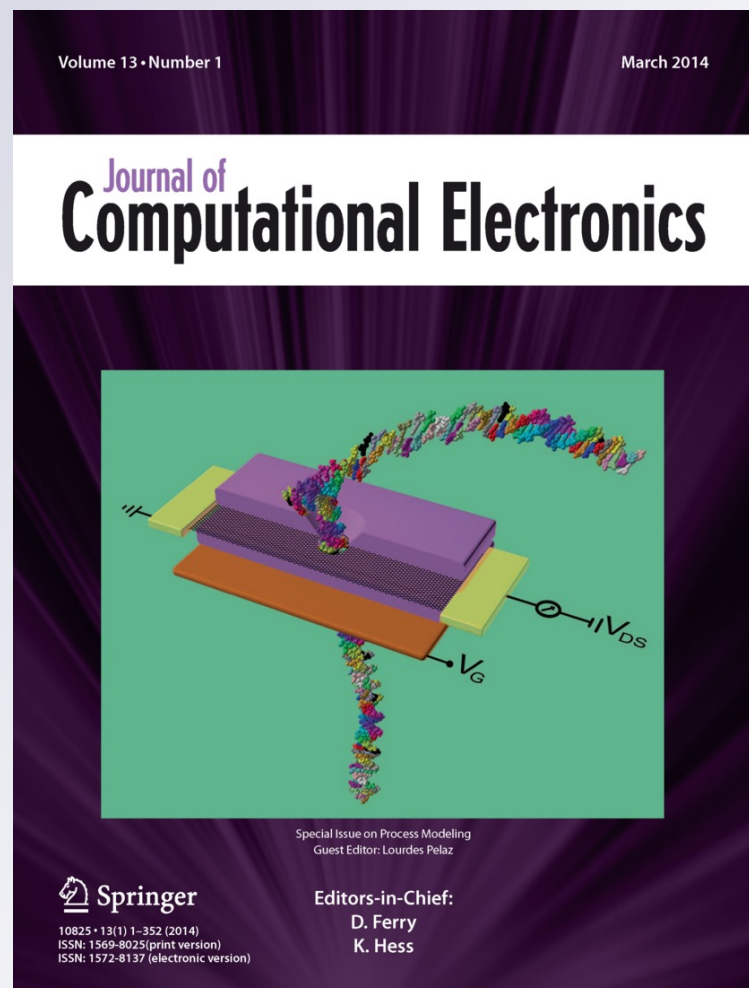
ISSN 1569-8025

Volume 13

Number 1

J Comput Electron (2014) 13:287-299

DOI 10.1007/s10825-013-0523-2



**Your article is protected by copyright and all rights are held exclusively by Springer Science +Business Media New York. This e-offprint is for personal use only and shall not be self-archived in electronic repositories. If you wish to self-archive your article, please use the accepted manuscript version for posting on your own website. You may further deposit the accepted manuscript version in any repository, provided it is only made publicly available 12 months after official publication or later and provided acknowledgement is given to the original source of publication and a link is inserted to the published article on Springer's website. The link must be accompanied by the following text: "The final publication is available at [link.springer.com](http://link.springer.com)".**

# Discrete geometric approach for modelling quantization effects in nanoscale electron devices

Alan Paussa · Ruben Specogna · David Esseni · Francesco Trevisan

Published online: 8 November 2013  
© Springer Science+Business Media New York 2013

**Abstract** This paper presents the solution of the Schrödinger–Poisson coupled problem for nanoscale electron devices obtained by means of the Discrete Geometric Approach (DGA). The paper illustrates a self-contained description of the DGA method for a Schrödinger–Poisson problem, discusses its implementation and compares the results of the DGA with respect to the ones obtained by the well established Pseudo-spectral (PS) method for two technologically relevant benchmark devices (i.e. a nanowire and a FinFET). Finally, the paper examines the merits of the DGA approach with respect to the Finite Differences (FD) and Finite Elements (FE), that are the most frequently used methods in the electron device community.

**Keywords** Discrete Geometric Approach (DGA) · Cell method · Pseudo-spectral method · Schrödinger–Poisson · Nanoscale electron devices · Nanowires · FinFETs

## 1 Introduction

The modern microelectronics and optoelectronics make use of semiconductor materials structured at truly nanometric

dimensions. Historical examples are related to High Electron Mobility Transistors (HEMT) based on III–V compound semiconductors. However also mainstream CMOS technologies have recently studied and fabricated transistors where the carrier transport is confined in very thin semiconductor layers. This is the case for fully depleted Silicon On Insulator (SOI) MOSFETs realized in silicon films thinner than 5 nm [1–4], and the trend has been reinforced by the INTEL announcement in spring 2011 concerning the introduction for the 22 nm technology node of Tri-Gate transistors (or FinFETs) [5], which are claimed to provide improved delays at a lower supply voltage with respect to planar devices.

Besides the progress related to new device architectures, the CMOS technology is undergoing remarkable innovations in terms of the optimization of the crystal orientation [6], of strain engineering in both planar and Tri-Gate transistors [7–9], and of introduction of channel materials alternative to silicon [10–14].

All the technology boosters mentioned above and related to crystal orientation, strain engineering and new channel materials affect the electrical characteristics of the MOSFETs essentially through the carrier band-structure, which form a quasi two-dimensional (2D) gas in MOS transistors, because there is a significant quantum confinement in at least one direction normal to the transport direction. Hence, accurate and efficient methods for the solution of the Schrödinger equation in nanoscale MOSFETs are a primary target for electron device modeling. In this respect, it is interesting to notice that the solution of the eigenvalue problem in a section of the device is a necessary step not only for semi-classical transport modeling based on either the momentum relaxation time approach [15–18] or the Monte Carlo method [19–22], but also for full quantum transport modeling, because, in order to reduce the huge computa-

---

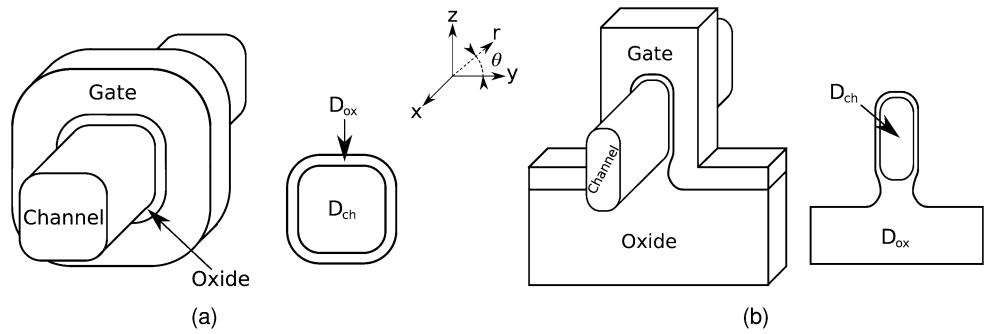
A. Paussa · R. Specogna (✉) · D. Esseni · F. Trevisan  
Department of Electrical, Mechanics and Management  
Engineering, University of Udine, via delle scienze 206,  
33100 Udine, Italy  
e-mail: [ruben.specogna@uniud.it](mailto:ruben.specogna@uniud.it)

A. Paussa  
e-mail: [alan.paussa@uniud.it](mailto:alan.paussa@uniud.it)

D. Esseni  
e-mail: [esseni@uniud.it](mailto:esseni@uniud.it)

F. Trevisan  
e-mail: [trevisan@uniud.it](mailto:trevisan@uniud.it)

**Fig. 1** Sketch of the two-dimensional domains considered in this work. In both the geometries, an inner silicon core  $D_{ch}$  is surrounded by the gate dielectric  $D_{ox}$



tional burden related to the calculation of the Green's functions in real-space, the calculations are typically performed by resorting to the mode space approach [23–26]. An interesting review of analytical and numerical methods for the solution of the Schrödinger equation in the effective mass approximation can be found in [27].

The aim of this paper is to explore the use of the Discrete Geometric Approach (DGA) [28–31] for the self-consistent solution of Schrödinger–Poisson coupled problem in the case of a 2D carrier confinement, relevant for nanowire FETs and FinFETs. Throughout the work we neglect any current flux at the gate terminal, hence we employ closed boundary conditions for the Schrödinger equation at the outermost boundary of the geometrical domain. Besides the formal presentation of the DGA method for the Schrödinger–Poisson coupled problem and its implementation, this paper presents also a systematic comparison between the results obtained with the DGA and the Pseudo-spectral (PS) [32–34] method for different electron device structures and different geometrical features.

The paper is organized as follows. We start, in Sect. 2, with the formulation of the quantization problem in nanodevices and in Sect. 3 we reformulate in a generalized way the Schrödinger–Poisson coupled problem. Then in Sects. 4, 5 and 6 we describe the DGA method, which highlights the geometric structure behind the Schrödinger–Poisson coupled problem. This idea has a solid physical and mathematical foundation, highlighted in the fundamental works of E. Tonti [30, 35], of A. Bossavit with the understanding of the geometric properties of the Finite Element Method in computational electromagnetics [36] or of T. Weiland regarding the Finite Integration Technique on electromagnetic wave propagation [37]. A formal convergence analysis has been presented in [38, 39] together with [40], which contains the evaluation of the constants bounding the approximation error. In Sect. 7 we show the numerical results for a nanowire FET and for a geometric configuration representative of an actually fabricated FinFET, and in Sect. 8 we finally draw the conclusions of our paper.

## 2 Formulation of the quantization problem in nanodevices

The quantization problem we consider occurs on a bi-dimensional domain  $D = D_{ch} \cup D_{ox}$  on a plane  $(y, z)$  normal to the transport direction  $x$ , where  $D_{ch}$ ,  $D_{ox}$  denote the channel and oxide domains respectively (see Fig. 1); the dimensions of the  $D_{ch}$  domains are some tens of nanometers and they will be precisely specified in the Numerical Results section. The surrounding gate electrode is modeled as an equipotential domain. In order to compute the electron density in narrow nanowires and FinFETs, the Effective Mass Approximation (EMA) model is typically used to describe the energy dispersion relation close to the conduction-band energy minima. Such a model leads to the following 2D Schrödinger equation in  $D$

$$-\text{div } q_\nu(\mathbf{r}) \text{ grad } \psi_{\nu,j}(\mathbf{r}) = \lambda_{\nu,j} \psi_{\nu,j}(\mathbf{r}) - u(\mathbf{r}) \psi_{\nu,j}(\mathbf{r}), \quad (1)$$

where  $\nu$  is the valley<sup>1</sup> index,  $\mathbf{r}$  is the position vector of a point individuated by the Cartesian components  $(y, z)$  of the position vector<sup>2</sup>  $\mathbf{r} \in D$  and  $\frac{\partial}{\partial x} = 0$  holds in the definition of the differential operators in Cartesian coordinates, thanks to the plane symmetry of the model;  $\psi_{\nu,j}(\mathbf{r})$  denotes the wave function<sup>3</sup> corresponding to the  $j$ -th eigenvalue  $\lambda_{\nu,j}$ . The  $q_\nu(\mathbf{r})$  is a diagonal<sup>4</sup> double tensor, whose Cartesian components in  $D$  are the inverse of effective masses for each valley index  $\nu$ ; for the  $ij$ -th Cartesian component (with  $i, j = 1, \dots, 3$ ), we write

$$q_{vij}(\mathbf{r}) = \frac{\hbar^2}{2m_{vi}(\mathbf{r})} \delta_{ij}, \quad (2)$$

where  $\hbar$  is the reduced Planck constant and  $m_{vi}(\mathbf{r})$  is the electron effective mass coefficient of the particle along the  $i$ -th

<sup>1</sup> A valley denotes a conduction-band energy minimum.

<sup>2</sup> Vectors and tensors are denoted in roman type.

<sup>3</sup> Wave functions must be normalized such that  $\int_D |\psi_{\nu,j}(\mathbf{r})|^2 ds = 1$ .

<sup>4</sup> In general,  $q_\nu(\mathbf{r})$  can also be non diagonal without affecting the results of this work.

axis (assumed here independent of  $\lambda_{v,j}$ ) and  $\delta_{ij}$  is the Kronecker symbol. Finally, the potential energy  $u(\mathbf{r})$  of an electron can be expressed as

$$u(\mathbf{r}) = -e\phi(\mathbf{r}) - \chi(\mathbf{r}), \tag{3}$$

where  $\phi(\mathbf{r})$  is electric scalar potential describing the electrostatic behavior of the nanodevice,  $e$  is the absolute value of electron charge and  $\chi(\mathbf{r})$  is the specified medium dependent energy affinity of the electron. Interface condition between  $D_{ch}$  and  $D_{ox}$  and boundary conditions on  $\partial D$  must be added to (1), in order to well pose the Schrödinger problem.

The electrostatic behavior of nanodevices at the equilibrium can be modeled by coupling to the Schrödinger problem (1) a Poisson problem for the electric scalar potential  $\phi(\mathbf{r})$

$$-\text{div} \epsilon(\mathbf{r}) \text{grad} \phi(\mathbf{r}) = \rho(\mathbf{r}), \quad \mathbf{r} \in D, \tag{4}$$

where  $\epsilon(\mathbf{r})$  denotes the medium permittivity double tensor;  $\rho(\mathbf{r})$  is the charge density given by

$$\rho(\mathbf{r}) = -e(N_A(\mathbf{r}) + n(\mathbf{r})), \tag{5}$$

where  $N_A(\mathbf{r})$  denotes the concentration of ionized acceptor atoms (as appropriate for  $n$ -type transistors), that is null in  $D_{ox}$ , and  $n(\mathbf{r})$  denotes the electron concentration in the conduction band. Boundary and interface conditions must be added to close the Poisson problem (4).

The coupling between the Schrödinger (1) and the Poisson (4) problems in  $D$  occurs as follows. On the one hand the electric scalar potential  $\phi(\mathbf{r})$  determines the potential energy  $u(\mathbf{r})$  in (3), on the other hand at the equilibrium the electron concentration  $n(\mathbf{r})$  in (4) is given by

$$n(\mathbf{r}) = \sum_v \sum_j N_{v,j} |\psi_{v,j}(\mathbf{r})|^2, \tag{6}$$

taking for  $N_{v,j}$  the appropriate expression for a quasi-1D electron gas in the effective mass approximation [41, 42]

$$N_{v,j} = g_v \sqrt{\frac{2m_x K_B T}{\pi \hbar^2}} \mathcal{F}_{-\frac{1}{2}} \left( \frac{E_F - \lambda_{v,j}}{K_B T} \right), \tag{7}$$

where  $g_v$  is the valley degeneracy,  $\mathcal{F}_{-\frac{1}{2}}$  is the complete Fermi–Dirac’s integral of order  $-1/2$  according to the Dingle notation [43],  $E_F$ ,  $K_B$  and  $T$  are Fermi level, Boltzmann constant and absolute temperature respectively.

### 3 The abstract Schrödinger and Poisson problems

Now we will reformulate the left hand side of the Schrödinger problem (1) in terms of the following relations

$$-\text{grad} \psi_{v,j}(\mathbf{r}) = \mathbf{a}(\mathbf{r}), \tag{8}$$

$$\mathbf{q}_v(\mathbf{r})\mathbf{a}(\mathbf{r}) = \mathbf{b}(\mathbf{r}), \tag{9}$$

$$\text{div} \mathbf{b}(\mathbf{r}) = \gamma(\mathbf{r}), \tag{10}$$

where we introduced in  $D$  the vector fields  $\mathbf{a}(\mathbf{r})$ ,  $\mathbf{b}(\mathbf{r})$  and the scalar field  $\gamma(\mathbf{r})$ , respectively; moreover the right hand side of (1) becomes

$$(\lambda_{v,j} - u(\mathbf{r}))\psi_{v,j}(\mathbf{r}) = \gamma(\mathbf{r}). \tag{11}$$

Of course, (8), (9), (10) and (11) are equivalent to (1).

Similarly, the Poisson problem (4) can be rewritten in  $D$  as

$$-\text{grad} \phi(\mathbf{r}) = \mathbf{E}(\mathbf{r}), \tag{12}$$

$$\epsilon(\mathbf{r})\mathbf{E}(\mathbf{r}) = \mathbf{D}(\mathbf{r}), \tag{13}$$

$$\text{div} \mathbf{D}(\mathbf{r}) = \rho(\mathbf{r}), \tag{14}$$

where we introduced the electric and displacement vector fields  $\mathbf{E}(\mathbf{r})$ ,  $\mathbf{D}(\mathbf{r})$  and the charge density  $\rho(\mathbf{r})$  is given by (5).

Due to the plane  $(y, z)$  symmetry of the Schrödinger and Poisson problems, the vector and scalar fields previously introduced are invariant along the transport direction  $x$ .

We observe that the differential structure of the Schrödinger and Poisson problems in  $D$  is identical, apart from the additional relation (11) specific of the Schrödinger problem only; thence, we may reformulate both the problems in a unified way as

$$-\text{grad} \alpha(\mathbf{r}) = \mathbf{v}(\mathbf{r}), \tag{15}$$

$$\mathbf{m}(\mathbf{r})\mathbf{v}(\mathbf{r}) = \mathbf{w}(\mathbf{r}), \tag{16}$$

$$\text{div} \mathbf{w}(\mathbf{r}) = \beta(\mathbf{r}), \tag{17}$$

$$\eta(\mathbf{r})\alpha(\mathbf{r}) = \beta(\mathbf{r}), \tag{18}$$

involving the pair of scalar fields  $\alpha(\mathbf{r})$ ,  $\beta(\mathbf{r})$ , the pair of vector fields  $\mathbf{v}(\mathbf{r})$ ,  $\mathbf{w}(\mathbf{r})$ ; relations (16) and (18) can be interpreted as *constitutive relations* between a pair of vector and scalar fields respectively,  $\mathbf{m}(\mathbf{r})$  and  $\eta(\mathbf{r})$  being the medium characteristics.

Clearly, by substituting the corresponding scalar and vector fields, (15)–(17) yield the Poisson problem, while (15)–(18) represent the Schrödinger problem.

Finally, boundary conditions on  $\partial D = S_D \cup S_N$  must be added to close the Schrödinger and Poisson problems; in general, Dirichlet and Neumann boundary conditions are imposed on the portions  $S_D$ ,  $S_N$  of  $\partial D$  respectively, by prescribing the values

$$(\alpha(\mathbf{r}))_{S_D}, \quad (\mathbf{m}(\mathbf{r})\text{grad} \alpha(\mathbf{r}) \cdot \mathbf{n}(\mathbf{r}))_{S_N}, \tag{19}$$

$\mathbf{n}(\mathbf{r})$  being the outward normal to  $\partial D$ . Moreover, the tensor  $\mathbf{m}(\mathbf{r})$  is usually discontinuous in  $D$ , which leads to the interface conditions on surface  $S_m$  separating subregions with

different material properties. In our coupled problem such a surface separates the  $D_{ch}$  and  $D_{ox}$  domains and we write

$$\begin{aligned}
 (\alpha(\mathbf{r}))_{S_m^+} &= (\alpha(\mathbf{r}))_{S_m^-}, \quad (\mathbf{m}(\mathbf{r})\text{grad}\alpha(\mathbf{r}) \cdot \mathbf{n}(\mathbf{r}))_{S_m^+} \\
 &= (\mathbf{m}(\mathbf{r})\text{grad}\alpha(\mathbf{r}) \cdot \mathbf{n}(\mathbf{r}))_{S_m^-}, \quad (20)
 \end{aligned}$$

where  $\mathbf{n}(\mathbf{r})$  is the normal to  $S_m$ ;  $S_m^+$ ,  $S_m^-$  denote the positive and negative sides of  $S_m$  respectively.

We will refer to the problem formulated in terms of the relations from (15) to (18) subject to (19), (20) as the *abstract problem*.

### 4 Discrete Geometric Approach

To discretize the abstract problem (15)–(18) we will rely on the geometrical structure behind a physical theory [35–37] by means of the DGA.

#### 4.1 Domain discretisation

We introduce in  $D$  a discretisation for the abstract problem. The discretisation consists of a primal *simplicial* cell complex  $\mathcal{K} = \{\mathcal{N}, \mathcal{E}, \mathcal{F}, \mathcal{V}\}$ , whose oriented geometrical elements are nodes  $n_i \in \mathcal{N}$ , edges  $e_j \in \mathcal{E}$ , faces  $f_h \in \mathcal{F}$ , and volumes  $v_k \in \mathcal{V}$  (triangular prisms), [35], Fig. 2. Due to the plane symmetry of the of the scalar and vector fields involved in our problem, a prism  $v_k$  has height  $h$  and  $v_k$  will be identified by its triangular base  $s_k$  laying in the plane of symmetry ( $y, z$ ); the fields are invariant for any plane parallel to the plane of symmetry and thus all the equations we will deduce will be independent of  $h$ .<sup>5</sup> The collection of all the triangles  $s_k$  yields to a triangular mesh in  $D$ . Similarly, the primal edges  $e_j$  of interest for our problem are only those laying on a ( $y, z$ ) symmetry plane. The cardinality of each set  $\mathcal{N}, \mathcal{E}, \mathcal{F}, \mathcal{V}$  is denoted by  $N, E, F$  and  $V$  respectively.

From the primal cell complex  $\mathcal{K}$ , we will construct a *barycentric* dual complex  $\tilde{\mathcal{K}} = \{\tilde{\mathcal{V}}, \tilde{\mathcal{F}}, \tilde{\mathcal{E}}, \tilde{\mathcal{N}}\}$ , whose oriented geometrical elements are dual nodes  $\tilde{n}_k \in \tilde{\mathcal{N}}$ , dual edges  $\tilde{e}_h \in \tilde{\mathcal{E}}$ , dual faces  $\tilde{f}_j \in \tilde{\mathcal{F}}$  and dual volumes  $\tilde{v}_i \in \tilde{\mathcal{V}}$ . According to the barycentric subdivision, a dual node  $\tilde{n}_k$  is the barycenter of the prism  $v_k$ , a dual edge  $\tilde{e}_h$  is a broken segment of line joining the barycenters of a pair of prisms through the barycenter of the face  $f_h$  they have in common. Due to the plane symmetry, we need only the dual faces  $\tilde{f}_j$  dual to the primal edges  $e_j$ , Fig. 2; such a dual face  $\tilde{f}_j$  is the union of the pair of rectangular faces, tailored within each of the pair of primal volumes (prisms) having the edge  $e_j$  in common. Again the height a dual face  $\tilde{f}_j$  is  $h$ . Finally, a

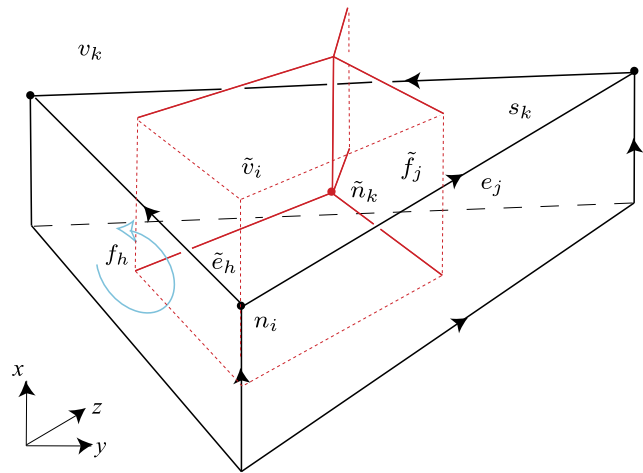


**Fig. 2** Oriented geometric elements of the primal complex  $\mathcal{K}$  and of the dual complex  $\tilde{\mathcal{K}}$  restricted, for clarity, to a single prism  $v_k$  whose base is the triangle  $s_k$  laying on the plane of symmetry

dual volume  $\tilde{v}_i$  is the union of a number of hexahedral sub-regions of height  $h$  tailored within each of the primal volumes (prisms) of the cluster of primal volumes having  $n_i$  as common node.

The cells of  $\mathcal{K}$  are by construction in a one-to-one correspondence<sup>6</sup> with those of  $\tilde{\mathcal{K}}$ , Fig. 2; The inner orientation of  $\mathcal{K}$  induces corresponding orientation [35] of  $\tilde{\mathcal{K}}$ . The interconnections of  $\mathcal{K}$  are described by incidence matrices; for our purposes, we need matrix  $\mathbf{G}$  of dimension  $E \times N$  of incidence numbers  $G_{ji}$  between the orientations of pairs  $(e_j, n_i)$  and matrix  $\tilde{\mathbf{D}}$  of dimension  $N \times E$  of incidence numbers between the orientations of pairs  $(\tilde{v}_i, \tilde{f}_j)$ ; thanks to the duality between  $\mathcal{K}, \tilde{\mathcal{K}}$   $\tilde{\mathbf{D}} = -\mathbf{G}^T$  holds.<sup>7</sup>

#### 4.2 Integral variables and their association to the elements of $\mathcal{K}, \tilde{\mathcal{K}}$

We introduce the array  $\mathbf{A}$  of dimension  $N$ , whose  $i$ -th entry  $A_i = \alpha(\mathbf{r}_{n_i})$ , is the value  $\alpha(\mathbf{r}_{n_i})$  assumes at the position  $\mathbf{r}_{n_i}$  of the node  $n_i$ , with  $i = 1, \dots, N$ . The circulation

$$V_j = \int_{e_j} \mathbf{v}(\mathbf{r}) \cdot d\mathbf{l} \quad (21)$$

of the vector  $\mathbf{v}(\mathbf{r})$  along a primal edge  $e_j$  is associated with primal edges, with  $j = 1, \dots, E$ ; the array  $\mathbf{V}$  they form has dimension  $E$ . The flux of the vector  $\mathbf{w}(\mathbf{r})$  across a dual face  $\tilde{f}_j$  is associated with dual faces, with  $j = 1, \dots, E$ . Due the plane symmetry of  $\mathbf{w}(\mathbf{r})$

$$\int_{\tilde{f}_j} \mathbf{w}(\mathbf{r}) \cdot d\mathbf{s} = h W_j \quad (22)$$

<sup>6</sup>It is often referred to as *duality*.

<sup>7</sup>The minus sign comes from the assumption that  $n_i$  is oriented as a sink, whereas the boundary of  $\tilde{v}_i$  is oriented by the outer normal.

<sup>5</sup>It can be assumed unitary.

holds,  $h$  being the height of  $\tilde{f}_j$  and  $W_j$  the flux per unit height independent of  $h$ ; the array  $\mathbf{W}$  formed by the  $W_j$  has dimension  $E$ . Finally, we introduce the volume integral of the scalar field  $\beta$  associated with a dual volume  $\tilde{v}_i$ , with  $i = 1, \dots, N$ . Due to the plane symmetry of  $\beta(\mathbf{r})$

$$\int_{\tilde{v}_i} \beta(\mathbf{r})dv = hB_i \tag{23}$$

holds,  $B_i$  being the volume integral per unit height independent of  $h$ ; we denote with  $\mathbf{B}$  the corresponding array formed by the  $B_i$ , of dimension  $N$ .

The arrays  $\mathbf{A}$ ,  $\mathbf{V}$ ,  $\mathbf{W}$  and  $\mathbf{B}$  of integral variables are often referred to as Degrees of Freedom (DoF). We observe that the arrays  $\mathbf{V}$ ,  $\mathbf{W}$  are one dual of the other being associated with dual geometric elements of the sets  $\mathcal{E}$ ,  $\tilde{\mathcal{F}}$  respectively; similarly for the pair  $\mathbf{A}$ ,  $\mathbf{B}$ , being associated with the dual geometric elements of the sets  $\mathcal{N}$ ,  $\tilde{\mathcal{V}}$  respectively.

### 4.3 Balance equations and constitutive relations

Now, according to algebraic topology [35], we can straightforwardly construct *exact* discrete counterparts of (15) and (17) respectively, independently of the media and the metric of the pair of cell complexes  $\mathcal{K}$ ,  $\tilde{\mathcal{K}}$  in  $D$  as

$$-\mathbf{GA} = \mathbf{V}, \tag{24}$$

$$-\mathbf{G}^T \mathbf{W} = \mathbf{B}. \tag{25}$$

A further step in the discretisation process is the computation of *approximated* discrete counterparts of the constitutive relations (16) and (18), which can be written respectively as

$$\mathbf{MV} = \mathbf{W} \tag{26}$$

$$\mathbf{NA} = \mathbf{B}, \tag{27}$$

where  $\mathbf{M}$  and  $\mathbf{N}$  are square matrices of dimension  $E$  and  $N$  respectively, depending on metric and media properties of the pair of cell complexes [35, 36, 44].

A discrete counterpart of the abstract problem is thus obtained by substituting (24) in (26) and, in turn, (26) in (25) and we write

$$\mathbf{G}^T \mathbf{MGA} = \mathbf{B} \tag{28}$$

which is a discrete counterpart of (15)–(17). We will compute in a purely geometric way both the so called stiffness matrix  $\mathbf{G}^T \mathbf{MG}$  on the left-hand side of (28) and the matrix  $\mathbf{N}$  in (27). We will show how the geometric approach we pursue allows an efficient computation of the  $\mathbf{G}^T \mathbf{MG}$  matrix directly, avoiding the storage and the multiplication of the single matrices  $\mathbf{M}$ ,  $\mathbf{G}$ ; moreover the geometric approach leads to a diagonal matrix  $\mathbf{N}$ .

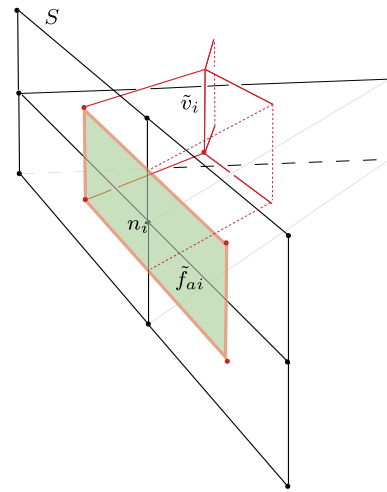


**Fig. 3** A portion of surface  $S$  is shown, representing, according to the case, either portions of  $S_D \cup S_N$  or  $S_m$ . An additional dual face  $\tilde{f}_{ai}$  in a one-to-one correspondence with node  $n_i$  on  $S_D \cup S_N$  or on  $S_m$  is also evidenced together with a portion of the corresponding dual volume  $\tilde{v}_i$

### 4.4 Discrete boundary and interface conditions

Discrete counterparts of Dirichlet boundary conditions (19) on the discretized portion  $S_D$  of the boundary are imposed by assigning the  $A_i$  values on the primal nodes  $n_i$  on  $S_D \subseteq D$ . Discrete Neumann boundary conditions on the discretized portion  $S_N \subset D$  are specified by assigning the values of  $W_{ai}$  associated with additional boundary dual faces  $\tilde{f}_{ai}$  on  $S_N$  in a one-to-one correspondence with the primal nodes  $n_i$  on  $S_N$ , Fig. 3; discrete homogeneous Neumann boundary conditions on  $S_N$  are naturally accounted for in (28) by assuming<sup>8</sup>  $W_i = 0$  on  $\tilde{f}_{ai}$ .

Discrete counterpart of interface condition on discrete discontinuity surface  $S_m$  in  $D$  is automatically accounted for due to the continuity of the circulations  $V_j$  along primal edges  $e_j$  on  $S_m$ ; this yields in turn the first of (20) which assures the continuity of the potential  $\alpha(\mathbf{r})$  on primal nodes belonging to  $S_m$ . Also the natural continuity of the flux  $W_{aj}$  across the two sides of each additional dual face  $\tilde{f}_{ai}$  on  $S_m$ , assures that the discrete counterpart of the second of (20) is implicitly satisfied.

## 5 Geometric construction of $\mathbf{G}^T \mathbf{MG}$ and $\mathbf{N}$ matrices

In the following, without losing generality, we will focus on a single triangle  $s_k$  corresponding to a prism  $v_k$  of height  $h$ , Fig. 2. With respect to  $s_k$ , we will compute the local stiffness matrix  $(\mathbf{G}^T \mathbf{MG})^k$  and the matrix  $(\mathbf{N})^k$ , with  $k = 1, \dots, V$ ; the corresponding global matrices  $\mathbf{G}^T \mathbf{MG}$  and

<sup>8</sup>This is to say that additional dual faces  $\tilde{f}_{ai}$  are not considered in the assembling process of (28).

$\mathbf{N}$  are then easily deduced, by adding the local contributions from each triangle of the complex according to a standard assembling process.

At the base of the computation there is the assumption of local *uniformity* of scalar, vector and tensor field quantities within each  $s_k$  with  $k = 1, \dots, V$ , since, within a small enough region, any regular field quantity can be approximated by a *uniform* field.

### 5.1 Computation of local stiffness matrix

We denote with  $n_i, i = 1, \dots, 3$ , a node of  $s_k$ , the cyclic index  $i$  being of modulo 3; we introduce the pair  $(e_i, f_{i-1})$  formed by a primal edge  $e_i$  and the not coplanar primal face  $f_{i-1}$  of  $v_k$ , having node  $n_i$  in common. Correspondingly,  $e_i, f_{i-1}$  denote the edge vector<sup>9</sup> and the face vector<sup>10</sup> associated with  $e_i, f_{i-1}$  respectively.

From the geometric interpretation of a pair of vectors forming a base in  $\mathbb{R}^2$  and the pair of vectors forming its *reciprocal* base, [45], the following, purely geometric, tensor identity

$$D_{ki-1} \tilde{f}_{i-1} \otimes G_{in_i} e_i + D_{ki} \tilde{f}_i \otimes G_{i-1n_i} e_{i-1} = 2\mathbf{I} |v_k|, \quad (29)$$

holds for prism  $v_k$ , where symbol  $\otimes$  denotes the tensor product,  $\mathbf{I}$  is the identity tensor,  $|v_k|$  is the volume of  $v_k$ ,  $G_{in_i}$  is the incidence number ( $\pm 1$ ) between the inner orientations of  $e_i$  and  $n_i$ , while  $D_{ki}$  is the incidence number ( $\pm 1$ ) between the inner orientations of  $v_k$  and  $f_i$ . Since

$$f_i = |e_i| h u_i, \quad |v_k| = |s_k| h \quad (30)$$

hold, where  $u_i = f_i / |f_i|$  is the unit vector normal to  $f_i$ , then by right multiplying (29) by the vector  $v(r)$  locally *uniform* in  $v_k$ , we obtain

$$v = \frac{1}{2|s_k|} (D_{ki-1} G_{in_i} |e_{i-1}| u_{i-1} V_i + D_{ki} G_{i-1n_i} |e_i| u_i V_{i-1}) \quad (31)$$

where we used (21).

Now, denoting with  $(n_i, n_{i+1})$  the boundary nodes of the edge  $e_i$ , with  $i = 1, \dots, 3$  and  $i$  modulo 3, then

$$G_{in_i} = -G_{in_{i+1}} \quad (32)$$

holds; using (24) for edge  $e_i$  and (32), we obtain

$$V_i = -G_{in_i} (A_{n_i} - A_{n_{i+1}}). \quad (33)$$

<sup>9</sup>It is the vector having as amplitude the length of the edge, directed and oriented as the edge.

<sup>10</sup>It is the vector having as amplitude the area of the face, normal to the face and oriented in a congruent way as the orientation of the face.

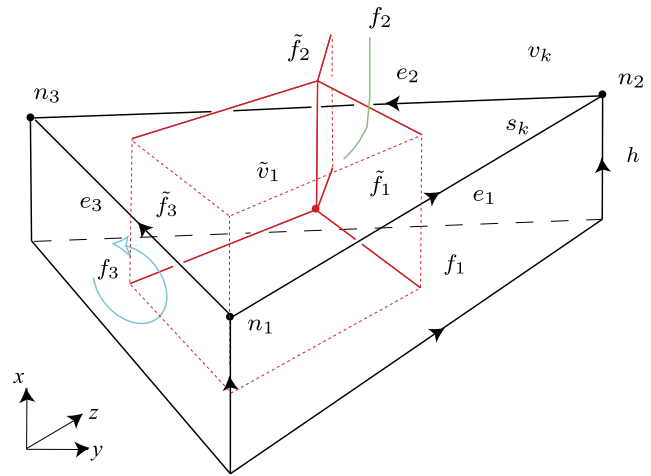


**Fig. 4** Geometric elements involved in the computation of local stiffness matrix for the triangle  $s_k$  (or prism  $v_k$ )

Substituting (33) for  $V_i$  in (31) and using (32), we write

$$v = \frac{1}{2|s_k|} (D_{ki-1} |e_{i-1}| u_{i-1} A_{n_{i+1}} + D_{ki} |e_i| u_i A_{n_{i-1}} - (D_{ki-1} |e_{i-1}| u_{i-1} + D_{ki} |e_i| u_i) A_{n_i}). \quad (34)$$

Since  $\sum_{i=1}^3 D_{ki} \tilde{f}_i = 0$  holds for the lateral face vectors of the prism  $v_k$ , from the first of (30) we write

$$\sum_{i=1}^3 D_{ki} |e_i| u_i = 0 \quad (35)$$

and (34) yields

$$v = \frac{1}{2|s_k|} \sum_{i=1}^3 D_{ki+1} |e_{i+1}| u_{i+1} A_{n_i}, \quad (36)$$

where the pairing between the vector<sup>11</sup>  $D_{ki+1} |e_{i+1}| u_{i+1}$  and the potential  $A_{n_i}$  associated with the opposite node is apparent, for  $i = 1, \dots, 3$  and  $i$  modulo 3.

Next, assuming a material tensor  $m(r)$  locally uniform in  $v_k$ , (16) implies also the local uniformity of  $w(r)$  in  $v_k$ , thence (22) yields

$$h W_i = \tilde{f}_i \cdot m v, \quad i = 1, \dots, 3, \quad (37)$$

where  $\tilde{f}_i$  is the area vector associated with dual face  $\tilde{f}_i$  in a one-to-one correspondence with  $e_i$ , with  $i = 1, \dots, 3$ , Fig. 4. By particularizing (25) for the dual volume  $\tilde{v}_i$ , we write<sup>12</sup>

$$-G_{n_i i} W_i - G_{n_i i-1} W_{i-1} = B_{n_i}, \quad (38)$$

<sup>11</sup>It is a face vector per unit  $h$ .

<sup>12</sup>The contributions due to the fluxes across the pair of portions of the primal faces intersecting  $\tilde{v}_i$ , are omitted, for they cancel out in the assembly process of the entire dual volume.

and substituting (37) for  $W_i$  (38) yields

$$-G_{n_i} i \tilde{f}_i \cdot m v - G_{n_i i-1} \tilde{f}_{i-1} \cdot m v = h B_{n_i}. \tag{39}$$

Since in the prism  $v_k$  the following geometric relation

$$-G_{n_i} i \tilde{f}_i - G_{n_i i-1} \tilde{f}_{i-1} = \frac{1}{2} D_{k i+1} f_{i+1} \tag{40}$$

holds,  $D_{k i+1}$  being the incidence number between  $v_k$  and the lateral face  $f_{i+1}$ , with  $i = 1, \dots, 3$  and  $i$  modulo 3, then (39) becomes

$$\frac{1}{2} D_{k i+1} f_{i+1} \cdot m v = h B_{n_i} \tag{41}$$

or equivalently from the first of (30) it follows

$$\frac{1}{2} D_{k i+1} |e_{i+1}| u_{i+1} \cdot m v = B_{n_i}. \tag{42}$$

By substituting in (42), (36) for  $v$ , we obtain

$$\frac{1}{4|s_k|} \sum_{j=1}^3 D_{k i+1} |e_{i+1}| u_{i+1} \cdot m D_{k j+1} |e_{j+1}| u_{j+1} A_{n_j} = B_{n_i}. \tag{43}$$

It is important to note, that (43) is an *exact* discrete counterpart of (15), (16), (17) in  $v_k$  (or equivalently in  $s_k$ ), provided that  $v(r)$ ,  $w(r)$ ,  $m(r)$  are locally *uniform* in  $v_k$  (or equivalently in  $s_k$ ).

Therefore, from (43), the entry  $(\mathbf{G}^T \mathbf{M} \mathbf{G})_{ij}^k$  of a local symmetric stiffness matrix for  $|v_k| = h|s_k|$ , expressed efficiently in a pure geometric way, is given by

$$\begin{aligned} & (\mathbf{G}^T \mathbf{M} \mathbf{G})_{ij}^k \\ &= \frac{1}{4|s_k|} D_{k i+1} |e_{i+1}| u_{i+1} \cdot m D_{k j+1} |e_{j+1}| u_{j+1}, \\ & i, j = 1, \dots, 3. \end{aligned} \tag{44}$$

### 5.2 Computation of local N matrix

We introduce in the prism  $v_k$  (or equivalently in  $s_k$ ) a scalar function  $f_i(r)$ , attached to a primal node  $n_i$ , defined as

$$f_i(r) = \begin{cases} 1 & \text{if } r \in \tilde{v}_i \\ 0 & \text{elsewhere,} \end{cases} \tag{45}$$

$\tilde{v}_i$  being the dual volume corresponding to  $n_i$ , Fig. 4. These base functions represent exactly a locally uniform scalar field  $\alpha(r)$  in  $v_k$  as

$$\alpha(r) = \sum_{j=1}^3 f_j(r) A_j. \tag{46}$$

Next, using constitutive equation (18), (23) yields

$$h B_i = \int_{\tilde{v}_i} \eta(r) \alpha(r) dv = h \int_{\tilde{s}_i} \eta(r) \alpha(r) ds, \tag{47}$$

where we used the plane symmetry of  $\beta(r) = \eta(r) \alpha(r)$  and  $\tilde{s}_i$  is the base of the dual volume  $\tilde{v}_i$ .

Since (47) is specific of the Schrödinger problem only, we particularize  $\eta(r) = \lambda_{v,j} - u(r)$  according to the actual constitutive relation (11); assuming a locally uniform field  $\alpha(r)$  in  $\tilde{s}_i$ , with  $i = 1, \dots, 3$ , as in (46), we rewrite (47) as

$$B_i = \sum_{j=1}^3 \left[ \lambda_{v,j} \int_{\tilde{s}_i} f_j(r) ds - \int_{\tilde{s}_i} f_j(r) u(r) ds \right] A_j \tag{48}$$

$$= \lambda_{v,j} \sum_{j=1}^3 \delta_{ij} \frac{|s_k|}{3} X_j - \sum_{j=1}^3 \delta_{ij} \int_{\tilde{s}_i} u(r) ds A_j, \tag{49}$$

where we used (45) and the geometric identity  $|s_k| = 3|\tilde{s}_i|$ , for  $i = 1, \dots, 3$ .

Therefore, from (49), the entry  $(\mathbf{N})_{ij}^k$  of a local diagonal matrix  $\mathbf{N}^k$  for tetrahedron  $v_k$ , expressed efficiently in a purely geometric way, is given by

$$(\mathbf{N})_{ij}^k = \delta_{ij} \frac{|s_k|}{3} \lambda_{v,j} - \delta_{ij} \int_{\tilde{s}_i} u(r) ds. \tag{50}$$

Such a relation, suggests to partition  $\mathbf{N}^k$  as the sum of a pair of local diagonal matrices

$$(\mathbf{N})^k = \lambda (\mathbf{N})'^k - (\mathbf{N}_u)^k, \tag{51}$$

whose entries are  $\delta_{ij} \frac{|s_k|}{3}$ ,  $\delta_{ij} \int_{\tilde{s}_i} u(r) ds$  respectively. In this paper, we will assume a uniform potential energy distribution  $u_k$  in each  $s_k$ ; therefore for the entries of  $(\mathbf{N}_u)^k$  we simply write  $\delta_{ij} \frac{|s_k|}{3} u_k$ .

## 6 Discrete formulated Schrödinger–Poisson problem

Now by substituting in the abstract problem the variables specific of the Schrödinger or of the Poisson problems and using the same discretisation of the domain  $D$ , we can easily deduce discrete counterparts of the Schrödinger–Poisson problem obtained according to the DGA approach.

### 6.1 The discrete problems according to DGA approach

From (28), (27) and using (51) a generalized eigenvalue problem is obtained for the Schrödinger problem, for triangle  $s_k$ , as

$$((\mathbf{G}^T \mathbf{M}_{qv} \mathbf{G})^k + (\mathbf{N}_u)^k) \Psi^k = \lambda_{v,j} (\mathbf{N})'^k \Psi^k, \tag{52}$$

$\Psi^k$  being a local array of the  $\psi_i^k$  values, with  $i = 1, \dots, 3$ , in the nodes of  $s_k$ ; the entries of the local stiffness matrix  $(\mathbf{G}^T \mathbf{M}_{q_v} \mathbf{G})^k$  are obtained from (44) by substituting  $q_v$  for the tensor  $m$ . Then by assembling the contributions from (52), for  $k = 1, \dots, V$ , we obtain the final global generalized eigenvalue problem

$$(\mathbf{G}^T \mathbf{M}_{q_v} \mathbf{G} + \mathbf{N}_u) \Psi = \lambda_{v,j} \mathbf{N}' \Psi, \tag{53}$$

where  $\mathbf{N}_u$  and  $\mathbf{N}'$  are the global diagonal matrices corresponding to the local ones in (51). Since  $\mathbf{N}'$  is diagonal and positive definite, then (53) can be easily transformed into a standard one and we may write

$$(\mathbf{N}')^{-1/2} (\mathbf{G}^T \mathbf{M}_{q_v} \mathbf{G} + \mathbf{N}_u) (\mathbf{N}')^{-1/2} \Psi' = \lambda_{v,j} \Psi', \tag{54}$$

where we set  $\Psi' = (\mathbf{N}')^{1/2} \Psi$ . We observe that there is no need to compute the matrix products in (54); it is enough to multiply each non-zero  $ij$ -entry of the sparse matrix  $(\mathbf{G}^T \mathbf{M}_{q_v} \mathbf{G} + \mathbf{N}_u)$  by  $(\mathbf{N}')_i^{-1/2} (\mathbf{N}')_j^{-1/2}$  with  $i, j = 1, \dots, N$ , where  $(\mathbf{N}')_i^{-1/2}$  denotes the  $i$ -th diagonal element of  $(\mathbf{N}')^{-1/2}$ .

Similarly, from (28), (27) a local Poisson problem is obtained, for triangle  $s_k$ , as

$$(\mathbf{G}^T \mathbf{M}_\epsilon \mathbf{G})^k \Phi^k = \mathbf{Q}^k, \tag{55}$$

$\Phi^k$  being a local array of the  $\Phi_i^k$  values, with  $i = 1, \dots, 3$ , in the nodes of  $s_k$ ; the entries of the local stiffness matrix  $(\mathbf{G}^T \mathbf{M}_\epsilon \mathbf{G})^k$  are obtained from (44) by substituting  $\epsilon$  for the tensor  $m$ . The  $i$ -th entry  $Q_i^k$  of the local array  $\mathbf{Q}^k$  is the charge obtained from (5) as

$$Q_i^k = \int_{\tilde{v}_i^k} \rho dv, \tag{56}$$

$\tilde{v}_i^k$  being the portion of the dual volume tailored in  $v_k$ . Then by assembling the contributions from (4), for  $k = 1, \dots, V$ , we obtain the final global Poisson problem

$$\mathbf{G}^T \mathbf{M}_\epsilon \mathbf{G} \Phi = \mathbf{Q}. \tag{57}$$

### 7 Numerical results

We solved the coupled Schrödinger and Poisson problem for a gate-all-around nanowire and for a FinFET. As reference for the DGA method, we considered the results obtained with the Pseudo-spectral (PS) approach [32–34]. The PS method approximates the unknown function  $\psi$  of the coupled problem by using algebraic or trigonometric polynomials. If the unknown function is sufficiently smooth, the PS method leads to an extremely fast decrease of the approximating error with respect to the degree of the interpolating polynomial.

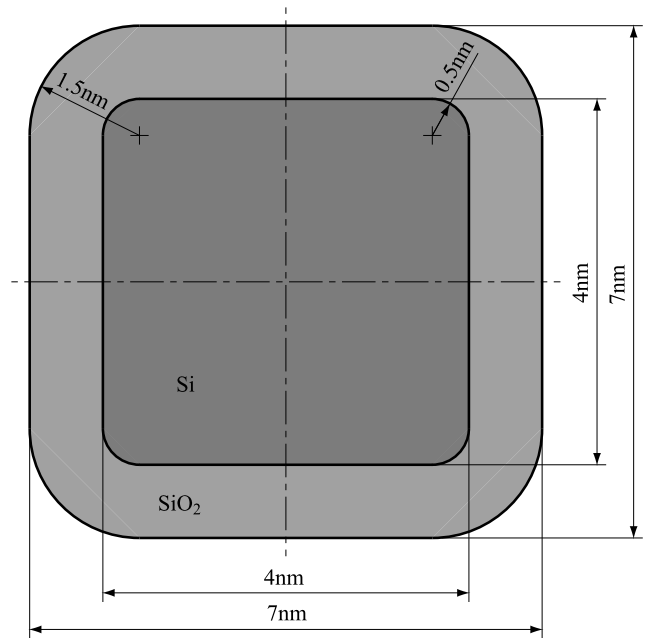


Fig. 5 The domain for the nanowire FET

A section of the simulated nanowire is sketched in Fig. 5, whereas Fig. 6 shows both a TEM picture of the FinFET device taken as a reference, and the corresponding geometrical domain actually used for the simulations. Here we would like to emphasize that the geometry of the FinFET has been obtained directly by tracing the image shown in Fig. 6c. For both the nanowire and the FinFET we denote with  $x$  the transport direction. In order to obtain an efficient convergence of the Schrödinger–Poisson iterative loop we employed the so called non-linear formulation of the Poisson equation described in [41, 42], for both the DGA and the PS method.

The solver for the Schrödinger–Poisson coupled problem by means of DGA method has been integrated into the GAME (Geometric Approach to Maxwell’s Equations) research code [46]. The software has been implemented in Fortran 90 and the Intel Fortran 90 Compiler has been used to produce the executable. The PARDISO direct solver contained in the Intel MKL scientific library has been employed to solve the resulting linear system of equations, whereas the FEAST [47] library has been used to solve the eigenvalue problems. The solver of the Schrödinger–Poisson coupled problem with the PS method has been implemented in MATLAB due to the presence of many built in functions that facilitate the implementation.

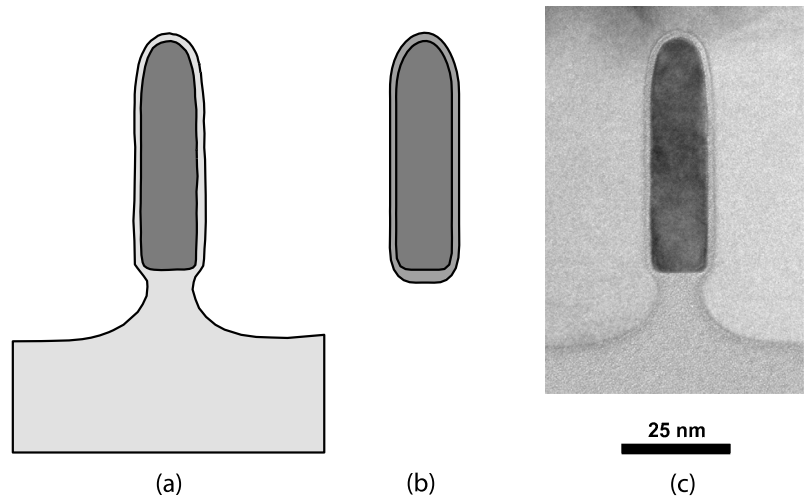
The Fermi energy  $E_F$  in Eq. (7) is taken as the zero of the energy and the temperature is set to  $T = 300$  K. The electron affinity  $\chi$  in Eq. (3) depends on the material and in silicon the  $\chi$  is 3.1 eV larger than in the oxide.

**Table 1** Expressions for the terms  $m_{vy}$ ,  $m_{vz}$  of the tensor  $q_v$  in Eq. (2) and for the corresponding effective mass  $m_x$  in the transport direction and the multiplicity of the valleys  $g_v$  (see Eq. (7)). The expressions are given for the [100] and the [110] transport directions and in terms

of the longitudinal  $m_l = 0.916$  and transverse  $m_t = 0.19$  masses of the silicon energy minima. The free electron mass is assumed to be  $m_0 = 5.68 \times 10^{-30} \text{ eV s}^2 \text{ nm}^{-2}$ . The index  $v$  denotes the different valleys

$x$	$y$	$z$	$\nu$	$\frac{m_0}{m_{vy}}$	$\frac{m_0}{m_{vz}}$	$m_x$	$g_v$
[110]	[110]	[00 $\bar{1}$ ]	1	$\frac{1}{m_t}$	$\frac{1}{m_l}$	$m_t$	2
			2	$\frac{m_t+m_l}{2m_t m_l}$	$\frac{1}{m_t}$	$\frac{m_t+m_l}{2}$	4
[100]	[010]	[001]	1	$\frac{1}{m_l}$	$\frac{1}{m_t}$	$m_t$	2
			2	$\frac{1}{m_t}$	$\frac{1}{m_l}$	$m_t$	2
			3	$\frac{1}{m_t}$	$\frac{1}{m_t}$	$m_l$	2

**Fig. 6** Simulation domains used for the FinFET problem (a) with DGA method (b) with PS method. The reference FinFET structure is illustrated in (c), that is a picture obtained with the Transmission Electron Microscopy (TEM) technique (courtesy of NXP Semiconductors, Leuven, Belgium)



7.1 Nanowire FET

A doping density  $N_A = 1 \times 10^{18} \text{ cm}^{-3}$  and an equivalent oxide thickness (EOT) of 1 nm have been considered in these simulations. The gate voltage  $V_G$  is used to specify the Dirichlet boundary conditions on the gate for the Poisson problem, while  $\psi_{v,j}(r) = 0$  for  $r \in \partial D$  is assumed for the Schrödinger problem. The diagonal entries of  $\epsilon(r)$  tensor are  $3.9\epsilon_0$  for  $r \in D_{ox}$  and  $11.7\epsilon_0$  for  $r \in D_{ch}$ ,  $\epsilon_0$  being the vacuum permittivity. The entries of the tensor  $q_v(r)$  are obtained by considering the [100] transport direction as described in Table 1.

Figure 7 shows the lowest eigenvalue versus the number of discretization points at  $V_G = 1 \text{ V}$ , and it can be seen that DGA and PS method converge to the same result; a similar behavior is observed for the total charge concentration  $n + N_A$  in Fig. 8. To complete the analysis of the relevant physical quantities internal to the device Fig. 9 finally illustrates a 3D view of the charge density distribution in the nanowire in the  $(y, z)$  plane calculated by the PS method.

As an example of an electrical quantity related to the overall device terminal characteristics, Fig. 10 shows a the total charge concentration  $n + N_A$  versus the gate voltage;

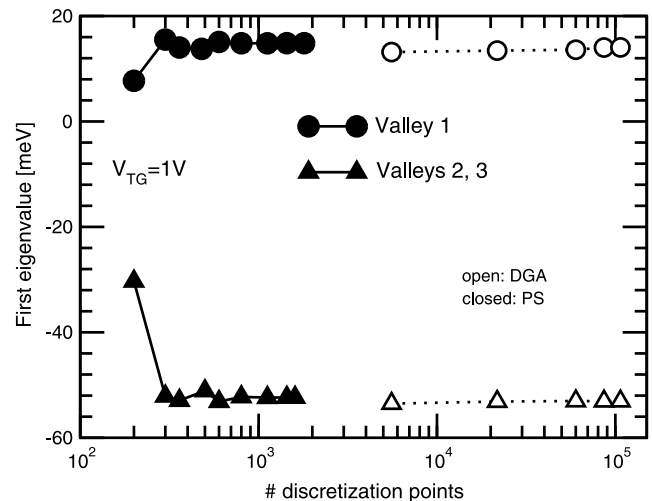


**Fig. 7** First eigenvalue for each valley versus the number of discretization points and for the nanowire FET; gate bias  $V_G = 1 \text{ V}$

as expected from the analysis of the internal quantities illustrated in Fig. 7 to 9, the linear charge density (i.e. integrated over the nanowire section) obtained with the two numerical methods is essentially the same.

7.2 FinFET

Figure 6c is a picture obtained by means of the Transmission Electron Microscopy (TEM) technique of the reference FinFET used in our simulations. In particular, Fig. 6a shows the geometry used in DGA simulations, while Fig. 6b illustrates the geometry used with the PS method. A doping density  $N_A = 1 \times 10^{15} \text{ cm}^{-3}$  and an equivalent oxide thickness of about 2 nm have been considered in these simulations. Figure 11 is a sketch illustrating the boundary conditions used for the Poisson problem in FinFETs: the gate voltage is used to specify the Dirichlet boundary conditions on the gate, while a homogeneous Neumann boundary condition is considered in the remaining parts. For the Schrödinger problem, instead, the boundary conditions were imposed by setting  $\psi_{v,j}(r) = 0$  for  $r \in \partial D$ . The diagonal entries of  $\epsilon(r)$  tensor are  $3.9\epsilon_0$  for  $r \in D_{ox}$  and  $11.7\epsilon_0$  for  $r \in D_{ch}$ ,  $\epsilon_0$  being the vacuum permittivity. The entries of the tensor  $q_v(r)$  are obtained by considering the  $[\bar{1}10]$  transport direction as described in Table 1.

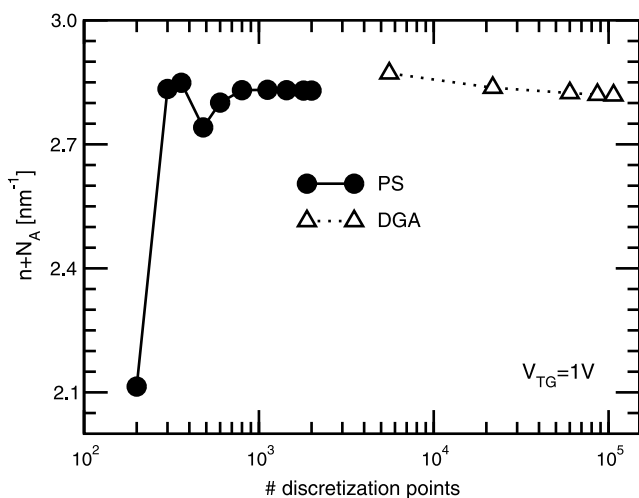


Fig. 8 Total charge concentration  $n + N_A$  in the nanowire FET versus the number of discretization points; gate bias  $V_G = 1 \text{ V}$

Fig. 11 Three different boundary conditions for the Poisson problem. The dashed parts of  $\partial D$  are subject to a homogeneous Neumann boundary condition

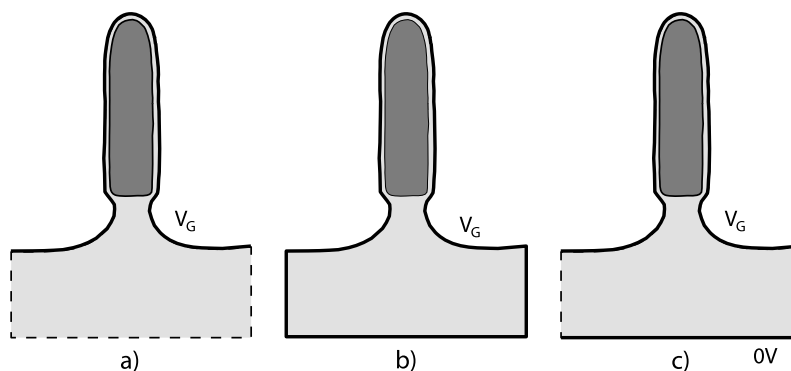


Figure 12 compares the convergence of lowest eigenvalue of the first and second valley for an increasing number of

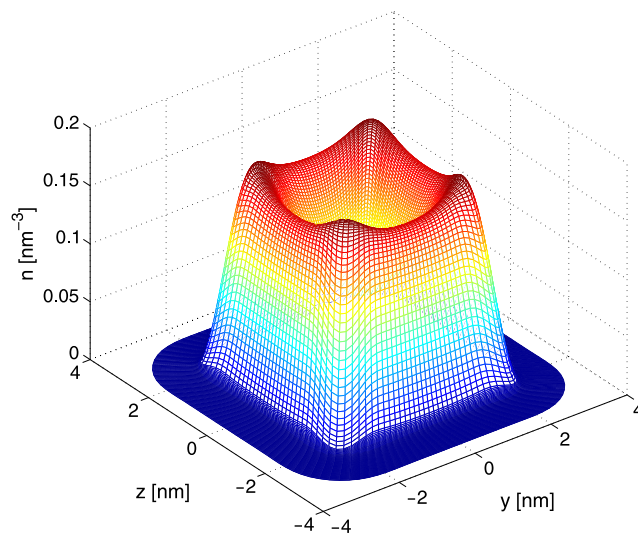


Fig. 9 A 3D view of the electron volumetric concentration  $n$  in the nanowire FET and computed with the PS method; gate voltage  $V_G = 1 \text{ V}$

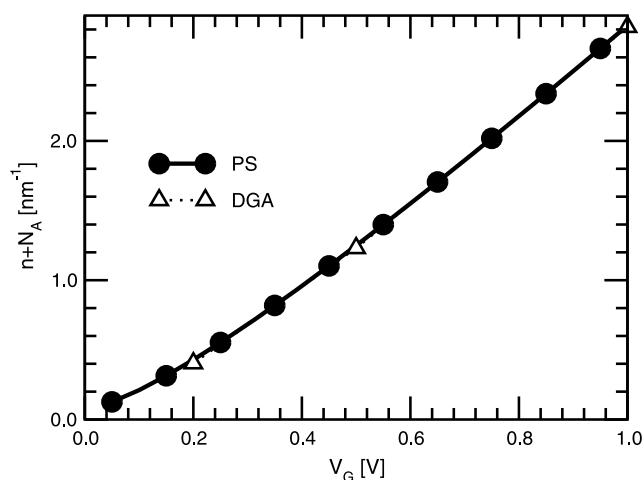


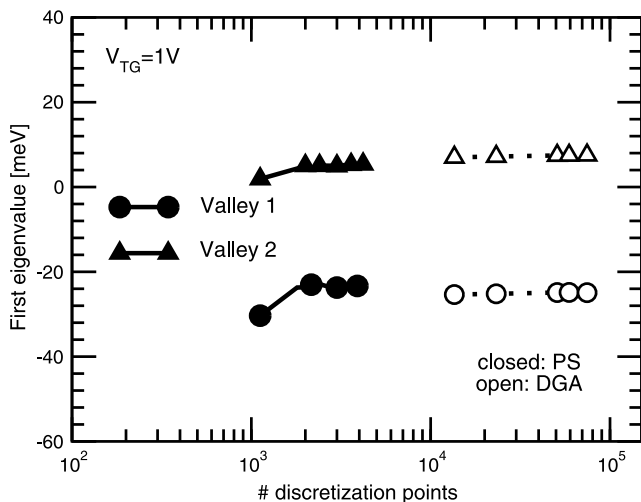
Fig. 10 Total charge concentration  $n + N_A$  versus gate voltage  $V_G$  for the nanowire FET

discretization points computed for both the DGA and the PS approaches. The corresponding total charge concentration  $n + N_A$  is illustrated in Fig. 13, while Fig. 14 reports a 3D view of the charge density distribution in a section of the FinFET and calculated by the PS method. Figure 15 finally shows the total charge concentration  $n + N_A$  variation with respect to the gate voltage  $V_G$ . The results obtained with the DGA and PS methods are similar but not exactly the same, due to the difference in the simulated domains shown in Fig. 6.

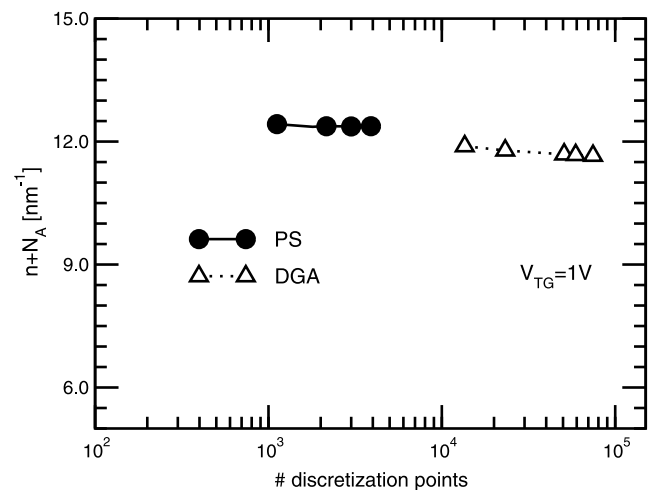
It is finally worth noting that, in case of DGA method, the size of the substrate oxide actually included in the simulated domain has an essentially negligible impact on the overall charge concentration. Such an impact remains negligible even when using different boundary conditions as the ones sketched in Fig. 11.

### 8 Conclusions

We have demonstrated that the DGA method can be used for the efficient solution of the Schrödinger–Poisson problem. The DGA, unlike classical Finite Differences (FD), can handle accurately complicated geometries like those of the real devices, and may be thus suitable for the study of the device variability produced by process induced variations of the geometrical dimensions. The DGA leads to a standard eigenvalue problem since the matrix  $N'$  in (53) is diagonal; on the contrary, in Finite Elements (FE) the matrix corresponding to  $N'$  in (53) is not diagonal, having the same sparsity pattern as the matrix on the left hand side of (53). Since first order FE and DGA have the same order of convergence, the latter is computationally more efficient because it saves memory (it saves exactly half of the memory, since the mass matrix has the same sparsity pattern as the left-hand-side matrix) and eigenvalue solvers for standard eigenvalue

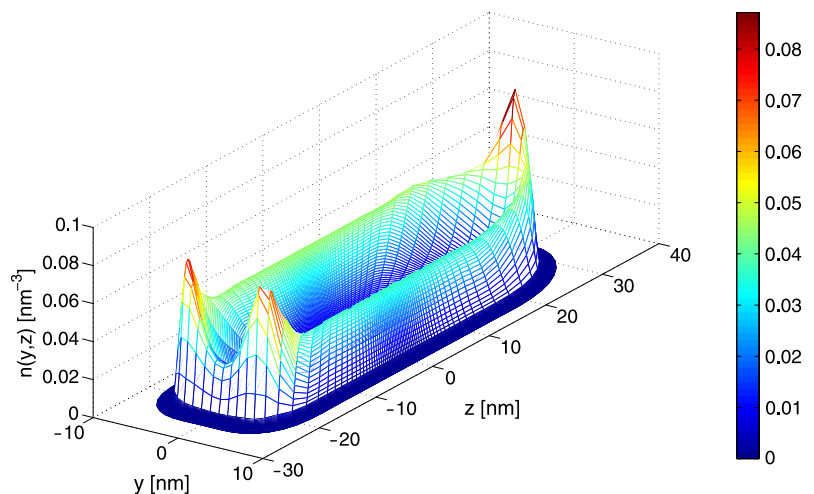


**Fig. 12** First eigenvalue for each valley versus the number of discretization points and for the FinFET transistor; gate bias  $V_G = 1$  V



**Fig. 13** Total charge concentration  $n + N_A$  versus the number of discretization points and in the FinFET transistor; gate bias  $V_G = 1$  V

**Fig. 14** A 3D view of the volumetric electron concentration  $n$  in the FinFET transistor obtained by the PS method; gate bias  $V_G = 1$  V



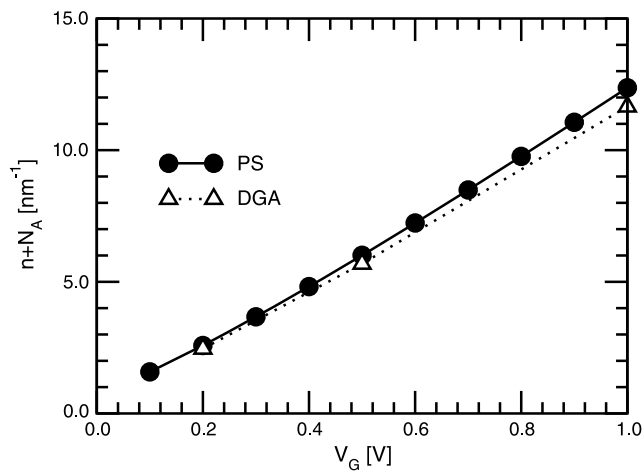


**Fig. 15** Total charge concentration  $n + N_A$  versus the gate voltage for the FinFET transistor

problems are faster than for generalized ones (generalized eigenvalue problems require a factorization of the mass matrix or the solution of a linear system for each iteration). Two benchmark devices, consisting in a nanowire FET and a FinFET, have been successfully simulated with the DGA method using as reference the Pseudo-spectral method; the results of the two approaches are in good agreement.

## References

- Esseni, D., Mastrapasqua, M., Celler, G.K., Fiegna, C., Selmi, L., Sangiorgi, E.: Low field electron and hole mobility of SOI transistors fabricated on ultra-thin silicon films for deep sub-micron technology application. *IEEE Trans. Electron Devices* **48**(12), 2842–2850 (2001)
- Esseni, D., Mastrapasqua, M., Celler, G.K., Fiegna, C., Selmi, L., Sangiorgi, E.: An experimental study of mobility enhancement in ultra-thin SOI transistors operated in double-gate mode. *IEEE Trans. Electron Devices* **50**(3), 802–808 (2003)
- Uchida, K., Koga, J., Ohba, R., Numata, T., Takagi, S.: Experimental evidences of quantum-mechanical effects on low-field mobility, gate-channel capacitance and threshold voltage of ultrathin body SOI MOSFETs. In: 2001 IEEE International Electron Devices Meeting (IEDM), pp. 633–636 (2001)
- Uchida, K., Watanabe, H., Kinoshita, A., Koga, J., Numata, T., Takagi, S.: Experimental study on carrier transport mechanisms in ultrathin-body SOI n- and p-MOSFETs with SOI thickness less than 5 nm. In: 2002 IEEE International Electron Devices Meeting (IEDM), pp. 47–50 (2002)
- <http://newsroom.intel.com/docs/DOC-2032>
- Yang, M., Chan, V.W.C., Chan, K.K., Shin, L., Fried, D.M., Stathis, J.H., Chou, A.I., Gusev, E., Ott, J.A., Burns, L.E., Fischetti, M.V., Jeong, M.: Hybrid-orientation technology (HOT): opportunities and challenges. *IEEE Trans. Electron Devices* **53**(5), 965–978 (2006)
- Thompson, S.E., Sun, G., Choi, Y.-S., Nishida, T.: Uniaxial-process-induced strained-Si: extending the CMOS roadmap. *IEEE Trans. Electron Devices* **53**(5), 1010–1020 (2006)
- Serra, N., Esseni, D.: Mobility enhancement in strained n-FinFETs: basic insight and stress engineering. *IEEE Trans. Electron Devices* **57**(2), 482–490 (2010)
- Conzatti, F., Serra, N., Esseni, D., De Michielis, M., Paussa, A., Palestri, P., Selmi, L., Thomas, S., Whall, T.E., Leadley, D.R., Parker, E.H.C., Witters, L., Hytch, M.J., Snoeck, E., Wang, T.J., Lee, W.C., Doornbos, G., Vellianitis, G., Dal van, M.J.H., Lander, R.J.P.: Investigation of strain engineering in FinFETs comprising experimental analysis and numerical simulations. *IEEE Trans. Electron Devices* **58**(6), 1583–1593 (2011)
- Rahman, A., Klimeck, G., Lundstrom, M.: Novel channel materials for ballistic nanoscale MOSFETs: bandstructure effects. In: 2005 IEEE International Electron Devices Meeting (IEDM), pp. 615–618 (2005)
- Pethe, A., Krishnamohan, T., Kim, D., Oh, S., Wong, H.S.P., Nishi, Y., Saraswat, K.C.: Investigation of the performance limits of III-V double-gate n-MOSFETs. In: 2005 IEEE International Electron Devices Meeting (IEDM), pp. 619–622 (2005)
- De Michielis, M., Esseni, D., Driussi, F.: Analytical models for the insight into the use of alternative channel materials in ballistic nano-MOSFETs. *IEEE Trans. Electron Devices* **54**(1), 115–123 (2006)
- Del Alamo, J.: Nanometre-scale electronics with III-V compound semi-conductors. *Nature* **479**, 317–323 (2011)
- Doornbos, G., Passlack, M.: Benchmarking of III-V n-MOSFET maturity and feasibility for future CMOS. *IEEE Electron Device Lett.* **31**, 1110–1112 (2010)
- Fischetti, M.V., Neumayer, D.A., Cartier, E.A.: Effective electron mobility in Si inversion layers in metal-oxide-semiconductor systems with a high-kappa insulator: the role of remote phonon scattering. *J. Appl. Phys.* **90**(9), 4587–4608 (2001)
- Esseni, D., Abramo, A.: Modeling of electron mobility degradation by remote Coulomb scattering in ultrathin oxide MOSFETs. *IEEE Trans. Electron Devices* **50**(7), 1665–1674 (2003)
- Esseni, D., Abramo, A., Selmi, L., Sangiorgi, E.: Physically based modeling of low field electron mobility in ultrathin single- and double-gate SOI n-MOSFETs. *IEEE Trans. Electron Devices* **50**(12), 2445–2455 (2003)
- Esseni, D.: On the modeling of surface roughness limited mobility in SOI MOSFETs and its correlation to the transistor effective field. *IEEE Trans. Electron Devices* **51**(3), 394–401 (2004)
- Jungemann, C., Edmunds, A., Engl, W.: Simulation of linear and nonlinear electron transport in homogeneous silicon inversion layers. *Solid-State Electron.* **36**(11), 1529–1540 (1993)
- Fischetti, M.V., Laux, S.E.: Monte Carlo study of electron transport in silicon inversion layers. *Phys. Rev. B* **48**(4), 2244–2274 (1993)
- Lucci, L., Palestri, P., Esseni, D., Bergagnini, L., Selmi, L.: Multisubband Monte Carlo study of transport, quantization and electron-gas degeneration in ultrathin SOI n-MOSFETs. *IEEE Trans. Electron Devices* **54**(5), 1156–1164 (2007)
- Esseni, D., Palestri, P., Selmi, L.: *Nanoscale MOS Transistors*. Cambridge University Press, Cambridge (2011)
- Venugopal, R., Goasguen, S., Datta, S., Lundstrom, M.S.: Simulating quantum transport in nanoscale transistors: real versus mode-space approaches. *J. Appl. Phys.* **92**(7), 3730–3739 (2002)
- Shin, M.: Full-quantum simulation of hole transport and band-to-band tunneling in nanowires using the  $k \cdot p$  method. *J. Appl. Phys.* **106**, 054505 (2009)
- Conzatti, F., Pala, M.G., Esseni, D.: Surface roughness induced variability in nanowire InAs tunnel-FETs. *IEEE Electron Device Lett.* **33**, 806–808 (2012)
- Conzatti, F., Pala, M.G., Esseni, D., Bano, E., Selmi, L.: Strain-induced performance improvements in InAs nanowire tunnel FETs. *IEEE Trans. Electron Devices* **51**(3), 2085–2092 (2012)
- Liu, Q.H., Cheng, C., Massoud, H.Z.: The spectral grid method: a novel fast Schrödinger-equation solver for semiconductor nanodevice simulation. *IEEE Trans. Comput.-Aided Des. Integr. Circuits Syst.* **23**(8), 1200–1208 (2004)

28. Specogna, R., Trevisan, F.: A discrete geometric approach to solving time independent Schrödinger equation. *J. Comput. Phys.* **230**, 1370–1381 (2011)
29. Breda, D., Esseni, D., Paussa, A., Specogna, R., Trevisan, F., Vermiglio, R.: Comparison between pseudospectral and discrete geometric methods for modelling quantization effects in nanoscale electron devices. *IEEE Trans. Magn.* **48**, 203–206 (2012)
30. Tonti, E.: On the formal structure of physical theories. In: *Quaderni dei Gruppi di Ricerca Matematica del CNR* (1975)
31. Codecasa, L., Specogna, R., Trevisan, F.: A new set of basis functions for the discrete geometric approach. *J. Comput. Phys.* **229**, 7401–7410 (2010)
32. Trefethen, L.N.: *Spectral Methods in MATLAB*. SIAM, Philadelphia (2000)
33. Heinrichs, W.: Spectral collocation schemes on the unit disc. *J. Comput. Phys.* **199**(1), 66–86 (2004)
34. Paussa, A., Conzatti, F., Breda, D., Vermiglio, R., Esseni, D., Palestri, P.: Pseudospectral methods for the efficient simulation of quantization effects in nanoscale MOS transistors. *IEEE Trans. Electron Devices* **57**(12), 3239–3249 (2010)
35. Tonti, E.: Algebraic topology and computational electromagnetism. In: *4th International Workshop on Electric and Magnetic Fields*, Marseille, France, 15 May, pp. 284–294 (1998)
36. Bossavit, A.: *Computational Electromagnetism*. Academic Press, San Diego (1998)
37. Weiland, T.: Time domain electromagnetic field computation with finite difference methods. *Int. J. Numer. Model.* **9**, 295–319 (1996)
38. Codecasa, L., Trevisan, F.: Convergence of electromagnetic problems modelled by discrete geometric approach. *Comput. Model. Eng. Sci.* **58**(1), 15–44 (2010)
39. Bonelle, J., Ern, A.: Analysis of compatible discrete operator schemes for elliptic problems on polyhedral meshes. *ESAIM: Math. Model. Numer. Anal.* (2013). doi:[10.1051/m2an/2013104](https://doi.org/10.1051/m2an/2013104)
40. Codecasa, L., Trevisan, F.: Error bounds for discrete geometric approach. *Comput. Model. Eng. Sci.* **59**(2), 155–179 (2010)
41. Trellakis, A., Galick, A.T., Pacelli, A., Ravaoli, U.: Iteration scheme for the solution of the two-dimensional Schrödinger–Poisson equations in quantum structures. *J. Appl. Phys.* **81**(12), 7880–7884 (1997)
42. Trellakis, A., Ravaoli, U.: Computational issues in the simulation of semiconductor quantum wires. *Comput. Methods Appl. Mech. Eng.* **181**(4), 437–449 (2000)
43. Blakemore, J.: Approximations for Fermi–Dirac integrals, especially the function used to describe electron density in a semiconductor. *Solid-State Electron.* **25**(11), 1067–1076 (1982)
44. Codecasa, L., Specogna, R., Trevisan, F.: Symmetric positive-definite constitutive matrices for discrete eddy-current problems. *IEEE Trans. Magn.* **42**(2), 510–515 (2007)
45. Gurtin, M.E.: *An Introduction to Continuum Mechanics*. Academic Press, San Diego (1981)
46. Specogna, R., Trevisan, F.: GAME (Geometric Approach to Maxwell's Equations) code. <http://www.comphys.com>. Copyright 2003–2012
47. Polizzi, E.: Density-matrix-based algorithms for solving eigenvalue problems. *Phys. Rev. B* **79**, 115112 (2009)